

# The influence of wavelength-dependent absorption and temperature gradients on temperature determination in laser-heated diamond-anvil cells

Jie Deng, Zhixue Du, Laura Robin Benedetti, and Kanani K. M. Lee

Citation: *J. Appl. Phys.* **121**, 025901 (2017); doi: 10.1063/1.4973344

View online: <http://dx.doi.org/10.1063/1.4973344>

View Table of Contents: <http://aip.scitation.org/toc/jap/121/2>

Published by the [American Institute of Physics](#)

---

---

# The influence of wavelength-dependent absorption and temperature gradients on temperature determination in laser-heated diamond-anvil cells

Jie Deng,<sup>1</sup> Zhixue Du,<sup>2</sup> Laura Robin Benedetti,<sup>3</sup> and Kanani K. M. Lee<sup>1</sup>

<sup>1</sup>Department of Geology and Geophysics, Yale University, New Haven, Connecticut 06520, USA

<sup>2</sup>Geophysical Laboratory, Carnegie Institution of Washington, Washington, DC 20015, USA

<sup>3</sup>Lawrence Livermore National Laboratory, Livermore, California 94550, USA

(Received 18 August 2016; accepted 15 December 2016; published online 9 January 2017)

*In situ* temperature measurements in laser-heated diamond-anvil cells (LHDACs) are among the most fundamental experiments undertaken in high-pressure science. Despite its importance, few efforts have been made to examine the alteration of thermal radiation spectra of hot samples by wavelength-dependent absorption of the sample itself and temperature gradients within the sample and their influence on temperature measurements while laser heating. In this study, we take (Mg, Fe)O ferropericlase as an example to evaluate the effects of these two factors. Iron-rich ferropericlase shows strong wavelength-dependent absorption in the wavelength range used to determine temperature, which, together with temperature gradients can account for largely aliased apparent temperatures in some experiments obtained by Wien fitting of detected thermal radiation intensities (e.g., an offset of  $\sim 700$  K for a 3300 K melting temperature). In general, wavelength-dependent absorption and temperature gradients of samples are two key factors to consider in order to rigorously constrain temperatures, which have been largely ignored in previous LHDAC studies. Published by AIP Publishing. [<http://dx.doi.org/10.1063/1.4973344>]

## I. INTRODUCTION

The laser-heated diamond-anvil cell (LHDAC) can simultaneously generate high pressures and high temperatures (up to a few 100 GPa and several 1000 K) while also allowing observation and *in situ* characterization of the sample. This technique is thus used to measure the material properties at extreme thermodynamic conditions. However, *in situ* temperature measurement remains inconsistent and controversial. Temperatures of LHDAC samples are determined by fitting the intensities emitted as thermal radiation to a Planck (or Wien) blackbody function (e.g., Ref. 1). There are two different methods to determine temperatures of laser-heated regions. For spectroradiometric approaches, intensities of light with wavelengths (usually) between 600 nm and 800 nm (e.g., Refs. 2 and 3) from a spatially selected area ( $\sim 4$   $\mu\text{m}$  in diameter for the narrow-slit method) on the heated sample is detected by a spectrometer. For multi-wavelength two-dimensional imaging radiometry,<sup>4,5</sup> intensities of radiation at four specific wavelengths (e.g., 580, 640, 766, and 905 nm)<sup>5</sup> across the heated region ( $\sim 50$   $\mu\text{m} \times 50$   $\mu\text{m}$ ) are collected to form a temperature map of the LHDAC sample. While the latter method yields measurements of temperature spatially in a LHDAC orthogonal to the laser, neither method yields information of temperature along the laser-heated axis.

Accurate temperature determination requires accurate detection of radiation intensity in both methods. However, the radiation intensities detected are not necessarily equal to those emitted by the hottest part of a heated sample. The alteration of radiation intensities by optical components,<sup>6</sup> i.e., system response, can be corrected by calibration using a known source of light, often a NIST-calibrated lamp (e.g., Newport Corp. 63358). However, there are still two other factors to consider even after taking into account the system

response. First is the temperature gradient within the sample. Diamond is an excellent thermal conductor and as a result, axial temperature gradients in laser-heated samples can reach up to several 1000 s K/ $\mu\text{m}$  depending on the thermal properties of materials, use of insulation layers, and sample thickness (e.g., Refs. 7 and 8). Radiation emitted from the sample is an accumulation of thermal radiation of the whole sample—not just the hottest part—even though the hottest part often dominates the shape of the thermal radiation spectrum. Correction for this effect requires the knowledge of the temperature profile within the LHDAC sample, which has been well established in previous studies (e.g., Refs. 9–12). The second factor is the wavelength-dependent absorption/emission throughout the sample. The uneven absorption of light at different wavelengths will also alter the thermal spectrum. This effect cannot be ignored when the absorption coefficient difference for the light of interest with different wavelengths becomes pronounced ( $\sim 1000$   $\text{cm}^{-1}$ ). Previous studies (e.g., Refs. 12–14) have noted that emissivity could be a cause of error in temperature measurements during LHDAC experiments. Moreover, Benedetti and Loubeyre<sup>11</sup> studied the error in the gray-body approximation due to wavelength-dependent emissivity for optically thick materials. However, there are few studies that account for both the absorption and emission process through materials during laser heating. The thermal radiation transfer process within samples during laser heating is governed by the radiative transfer equation (RTE), in which Kirchoff's law is considered and described below. As a result, temperature measurement for LHDAC experiment is essentially the well-studied inverse radiation problem,<sup>15–17</sup> i.e., to deduce difficult-to-measure parameters (i.e., temperature) based on measurements of the radiative intensity or radiative flux.

In this study, we evaluate the influences of axial temperature gradients and wavelength-dependent absorption/emission in temperature determination to better constrain the uncertainty of temperature measurements in LHDAC experiments. Additionally, we have constructed the temperature profiles of samples based on their cross sections (e.g., Fig. 2(a) in Ref. 7) which show how LHDAC samples can form layers of varying absorption which, in turn, affect temperature measurements. In the second half of this paper, a new method to more rigorously quantify the temperatures in LHDAC experiments is suggested by taking into consideration both the temperature gradients and wavelength-dependent absorption.

## II. GOVERNING EQUATIONS

### A. Axial temperature gradients

Both radial and axial temperature gradients exist within a laser-heated sample. Radial temperature gradients have been measured in some previous studies,<sup>18,19</sup> while direct measurement of axial temperature is still impossible. Instead, numerical modeling has been implemented to estimate the axial temperature gradient.<sup>10,20,21</sup> Following the same arguments given by Ref. 20, a 1D axial temperature gradient for the case where melt is present is obtained by solving the following steady state heat flow equation with an internal heating term,  $H$ :

$$\kappa \frac{d^2 T}{dz^2} + H = 0, \quad (1)$$

where  $\kappa$  is the thermal conductivity of the sample, and  $T$  is the temperature. The boundary conditions are (1) temperature at the diamond/sample interface is 300 K as diamonds are excellent thermal conductors; (2) temperature at the melt/solid interface is the melting temperature and also the maximum in the system,  $T_m$ ; and (3) melt is isothermal at  $T_m$ .

### B. Radiative heat transfer

At thermodynamic equilibrium,  $dI_\lambda$ , the change of spectral radiation intensity at a certain wavelength at normal incidence after passing through an absorbing-emitting (but not scattering medium) with thickness  $dz$  is composed of two terms. The first term is the absorption loss,  $-k_\lambda I_\lambda dz$ , where  $k_\lambda$  is the absorption coefficient, and  $I_\lambda$  is the intensity of radiation. The second term is the emission, which serves as the source of radiation. The efficiency of absorption at a specific wavelength is equal to the efficiency of emission according to Kirchoff's law. We thus have the following RTE to describe the intensity of radiation:

$$\frac{dI_\lambda}{dz} = -k_\lambda I_\lambda + k_\lambda E_\lambda, \quad (2)$$

where  $E_\lambda$  is the hemispherical spectral emissive power.  $E_\lambda = \pi B_\lambda$ , where  $B_\lambda$  is the blackbody spectral intensity determined by the Planck function

$$B_\lambda = \frac{2hc^2}{\lambda^5} \frac{1}{e^{\frac{hc}{\lambda k_B T}} - 1}, \quad (3)$$

where  $\lambda$  is the wavelength, and  $T$  is the temperature. The constants  $\pi$ ,  $h$ ,  $c$ , and  $k_B$  are pi, Planck's constant, the speed of light, and Boltzmann's constant, respectively. Scattering effects are grain size sensitive and scattering coefficient values under simultaneous high pressures and temperatures are very scarce. Besides, for many Earth materials, the scattering effects alter the radiation intensities by less than 4%, thus can be neglected to first order.<sup>22,23</sup>

The general solution to Eq. (2) for parallel planes with transparent boundaries is

$$I_\lambda(d) = I_\lambda(0)e^{-\int_0^d k_\lambda(z)dz} + \int_0^d k_\lambda E_\lambda e^{-\int_z^d k_\lambda(z')dz'} dz, \quad (4)$$

where  $I_\lambda(0)$  is the radiation intensity coming into the sample, and  $d$  is the thickness of materials that participate in the radiative heat transfer at the wavelengths of interest. For LHDAC experiments, intensities of light between  $\sim 600$  and  $900$  nm are generally utilized to determine the temperature. So the corresponding materials that participate in the radiative heat transfer in this wavelength range are the materials in between the two diamonds, including the pressure medium and sample.

If both  $k_\lambda$  and  $E_\lambda$  are constant with respect to  $z$ , then there are no radiation sources below the starting surface ( $I_\lambda(0) = 0$ ), and Eq. (4) can be simplified into

$$I_\lambda(d) = E_\lambda(1 - e^{-\tau_\lambda}), \quad (5)$$

where  $\tau_\lambda = \int_0^d k_\lambda dz$  is the optical thickness of the sample. If  $\tau_\lambda$  tends toward infinity (either  $k_\lambda$  or  $d$  or both are large), then the sample can be treated as a blackbody.

### C. Wien fitting

Intensities of radiation (at wavelengths 580, 640, 766, and 905 nm) emitted from a sample can be determined using Eq. (4). With the radiation intensities of at least two wavelengths (for multi-wavelength two-dimensional imaging radiometry, four wavelengths are used, while for spectroradiometric approaches, a continuous range of wavelengths are used), we are able to fit  $I_\lambda(d)$  with the Wien function

$$Wien = \frac{k_B}{hc} \ln \left( \frac{2\pi hc^2}{I_\lambda^5} \right) = \frac{1}{\lambda T} - \frac{k_B}{hc} \ln \epsilon. \quad (6)$$

Notice that here the gray-body approximation is used and  $\epsilon$  is the wavelength-independent emissivity of the gray-body. We define the temperature of the sample calculated by fitting the intensities of  $I_\lambda(d)$  to the Wien function as the apparent temperature,  $T_a$ .

## III. LHDAC EXPERIMENTS

### A. Method

Samples were loaded without any pressure transmitting medium into LHDACs equipped with  $300 \mu\text{m}$  culets and

rhodium gaskets which were pre-indented to a thickness of  $\sim 20\text{--}30\ \mu\text{m}$  (Fig. 1). Samples of polycrystalline ferroperricite  $\text{Mg}_{1-x}\text{Fe}_x\text{O}$  ( $x=0.12, 0.19$ , i.e.,  $\text{Mg}\# = 100 \times \text{Mg}/(\text{Mg}+\text{Fe})$ ) with different Mg# (88, 81) were synthesized from powders of  $\text{Fe}_2\text{O}_3$  and fired MgO as described elsewhere.<sup>7,24</sup> Pressurized samples were heated from one side with a near-infrared (NIR) laser (100 W, 1070 nm water-cooled fiber laser). We used predefined ramped laser heating to melt the sample: the laser is set to a low power for 2 s and then linearly ramped up to a peak power every 20 ms within 1 s and kept at the peak power for 0.5–1 s before turned off (e.g., Ref. 7). A mechanical shutter is opened  $\sim 40\text{--}100$  ms before the laser is quenched to allow the temperature measurement of the sample at peak power. Temperature distributions were measured by 4-color multi-wavelength imaging radiometry. Images of the laser-heated spot were collected simultaneously at 580, 640, 766, and 905 nm and spatially correlated.<sup>5</sup> At each position, a four-color fit was made with the Wien function using the gray-body approximation to construct the emissivity and temperature distributions of the hot spot in two dimensions. The two-dimensional, 4-color multi-wavelength imaging radiometric technique coupled with laser heating has been used to determine the phase diagram of ferroperricite at pressures up to 40 GPa (Ref. 7) and the melting temperature of four transition metals at room pressures and Re at high pressures.<sup>5</sup>

Other experimental details are further elaborated in Ref. 7. It should be emphasized that the criteria for melting used in this study is the quench texture and element distribution after heating.<sup>7</sup> In LHDAC experiments where the multi-wavelength imaging radiometric technique is used to measure temperature, the discontinuous change in emissivity is often correlated with the post-heating determination of melt location, and that region is also typically associated with the highest temperature in the sample. As such, a discontinuous change in emissivity versus temperature during laser heating is used to check consistency in melting identification (e.g., Ref. 4).

The emissivity values were obtained by fitting the thermal radiation to the gray-body approximation equation. While the discontinuous change in emissivity has been used to determine the melting temperature (e.g., Refs. 1 and 2), there is no physical reason why this correlation exists. The actual emissivity values at specific wavelengths can be quite different from those wavelength-independent fitting parameters as shown by Benedetti and Loubeyre.<sup>11</sup> In other words, the

emissivity values in the 2D emissivity maps do not have explicit physical meaning even though they are somehow correlated to the actual emissivity through the gray-body approximation. Additionally, the actual phase (liquid/solid) dependence of the emissivity at their melting points under high pressure and temperature is poorly understood. For some materials, no sudden change (even no change) of the spectral emissivity in certain wavelength ranges has been observed.<sup>5,25</sup> For example, the emissivity measurement by Watanabe *et al.*<sup>25</sup> indicated that there is no sudden change in the spectral emissivity of iron, cobalt, and nickel over a wavelength range from 650 to 800 nm upon melting at ambient pressure. To summarize, it is in principle an overuse of the fitted emissivity to correlate the emissivity map with the temperature map and optical image. But an emissivity map can be used as complementary information to check consistency in melting identification since it typically, but not always, corresponds well with the respective optical image and temperature map.

Quenched samples were cut and polished through the center of the heated region by Electrical Discharge Machining (EDM) and Focused Ion Beam (FIB) techniques, and then quantitatively analyzed by electron probe micro-analysis (EPMA) using wavelength or energy dispersive spectroscopy (WDS or EDS).<sup>7</sup> Thicknesses of the quenched samples ( $\sim 15\text{--}20\ \mu\text{m}$ ) were measured based on the polished cross sections.

## B. Results

Melting experiments of ferroperricite at 51 GPa (May2715C), 60 GPa (Jul0415), and 66 GPa (May2915) have been conducted; optical images and 2-D emissivity and temperature maps across the heated regions are shown in Fig. 2. The three images for sample May2715C are concentric. Regions I, II, and III in the optical images are determined from the quenched texture in each sample's cross-section and the optical images. Molten region (I) appears darker because of the higher iron content in the optical images. It correlates with the center of the Gaussian shaped laser and displays a higher apparent temperature compared to the surrounding coexisting solid (II) and starting materials (III). It should be noted that values shown in the emissivity map are the wavelength-independent emissivity of a gray-body (Eq. (6)) and can be quite off from the real emissivity values.<sup>11</sup> But as discussed above, discontinuous changes in these gray-body emissivity values typically correspond well with the initiation of melting and thus not a surprise that emissivity maps are concentric with their corresponding temperature maps. The contour drawn is partly based on the cross section across the dashed line. While there is a near 1:1 relationship between the optical images and emissivity map of sample May2915 (Figs. 2(g) and 2(h)), the 2-D temperature map (Fig. 2(i)) does not correspond to the emissivity map. The offsets of temperature maps are caused by areas in region II that appear to be "hotter" than region I. Region II is expected to be lower in temperature than region I because region II is not molten. The reason why this discrepancy occurs will be explained in Secs. IV–V.

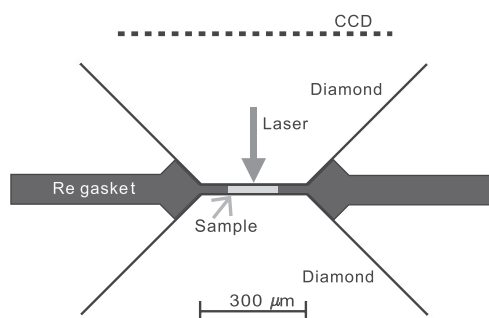


FIG. 1. Schematic of the LHDAC sample assembly used in this study.

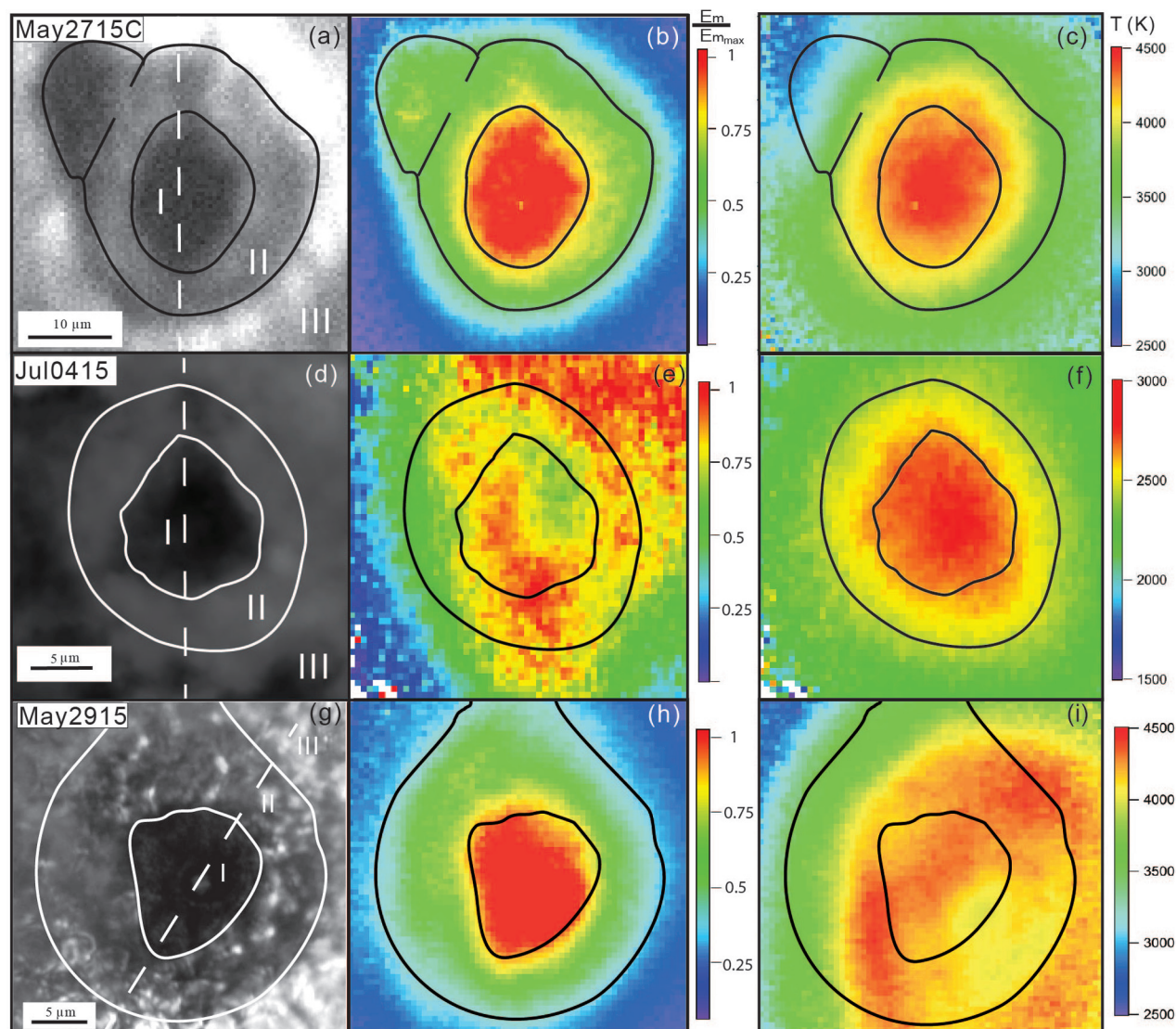


FIG. 2. Melting of ferropericlase ( $\text{Mg}_{0.88}, \text{Fe}_{0.12}\text{O}$ ) at 51 GPa (May2715C) and 66 GPa (May2915), ( $\text{Mg}_{0.81}, \text{Fe}_{0.19}\text{O}$ ) at 60 GPa (Jul0415). (a), (d), (g) Optical images; Regions I, II, and III are molten area, coexisting solid, and starting material, respectively. Dashed lines in optical images are the cross section positions. (b), (e), (h) The emissivity maps (the color scales correspond to the emissivity normalized by the maximum fitted emissivity); (c), (f), (i) are the temperature maps.

#### IV. FORWARD MODELING

In order to understand the reason for the offset between the apparent temperature map and optical image for sample May2915 and to also explore the influences of temperature gradients, wavelength-dependent absorption and emissivity on temperature measurements, forward modeling was conducted by considering a typical self-insulated sample configuration upon melting when laser-heated from one side (Fig. 3(a)). The melt has a paraboloidal upper surface on the laser-heated side and a flat lower surface on the non-heated side of the LHDAC corresponding to a typical melt shape obtained in the melting experiments (e.g., Fig. 2(a) in Ref. 7). The shortest distance from the paraboloid to the diamond anvil is  $1 \mu\text{m}$ , corresponding to the center of the laser beam. The total sample thickness is  $15 \mu\text{m}$ . The melt is assumed to be homogeneous both chemically and thermally.<sup>7</sup> Other set-up parameters are shown in Fig. 3(a).

##### A. Errors introduced by Wien fitting

It is well known that Wien fitting itself can introduce some errors to temperature measurements, as compared to Planck fitting, especially at temperatures above  $\sim 4000 \text{ K}$ . To quantify those errors, we assume that the whole sample is isothermal and the emissivity equals 1 at all wavelengths and denote the corresponding temperature profile as *Wien fit*. As shown by *Wien fit* in Fig. 3(c), the offset is small but increases with temperature, up to  $\sim 2\%$  at  $5000 \text{ K}$ .

##### B. Effects of the axial temperature gradient ( $T \text{ grad}$ )

The axial temperature gradient is obtained by solving Eq. (1). The solution for the sample configuration across the dashed line in Fig. 3(a) is shown in Fig. 3(b). Two sets of  $T_a$  for the center part of the sample (*Wien fit* and  $T \text{ grad}$ , see Fig. 3 for the definitions) are plotted against  $T_m$  in Fig. 3(c).

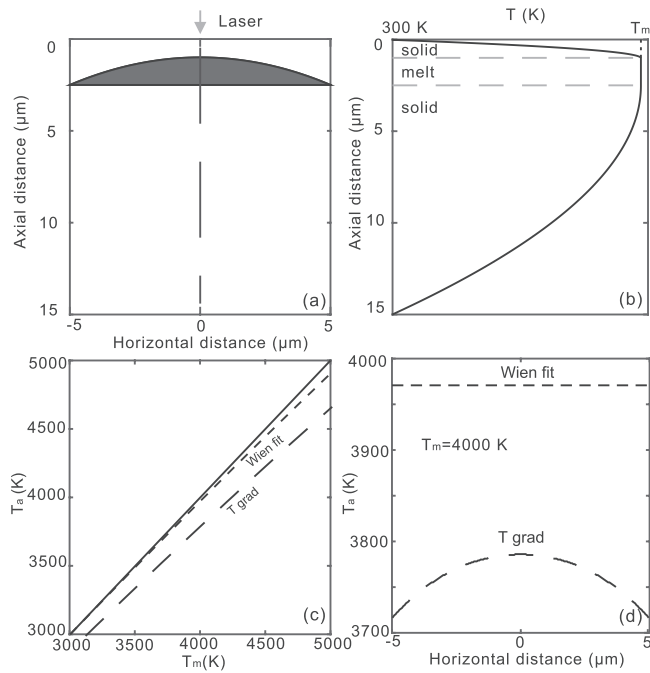


FIG. 3. Correlation between apparent melting temperature  $T_a$  and the real melting temperature  $T_m$  considering the effects of temperature gradient only. (a) Sample configuration: the dark part is melt and the others are solids. (b) Temperature profile across the center of the sample. (c) For the central part of the sample,  $T_a$  as a function of  $T_m$  when the temperature profile is as shown in (b) ( $T_{grad}$ , the corresponding to the apparent temperature profile when  $k_\lambda$  is constant throughout the sample, and  $\tau_\lambda$  is 1 for 580, 640, 766, and 905 nm and the sample is under the temperature profile in (b)). The difference between the solid thin diagonal line and *Wien fit* is the error induced solely by the Wien fitting. (d) Horizontal  $T_a$  profile across the center of the sample when  $T_m = 4000$  K. The *Wien fit* to  $T_m = 4000$  K is shown as a comparison.

For the  $T_{grad}$  case, we consider that axial temperature gradients exist within the sample and assume the wavelength-independent absorption coefficient values. An infinitely large  $k_\lambda$  value is not appropriate here because it will make the  $T_a$  close to the surface temperature as the radiation inside the sample is all absorbed by the surface.  $T_a$  with an axial temperature gradient  $T_{grad}$  deviates from  $T_m$  gradually as the  $T_m$  increases, indicating that the influence of temperature gradients on melting temperature determination is large and cannot be ignored when  $T_m$  is large. The horizontal  $T_a$  profile across the center of the sample shows a parabolic shape with the highest  $T_a$  in the center of the sample (positive parabola), because more hot melt is present in the regions closer to the center.

### C. Effects of wavelength-dependent absorption

Although generally more than two wavelengths are used to determine temperature in LHDAC experiments, radiation intensities of two wavelengths are theoretically sufficient to calculate temperature by the Wien approximation (Eq. (6)). In order to evaluate the influences of the absolute values of the absorption coefficients and differences between absorption coefficients of different wavelengths, we first only consider using intensities of light at

two wavelengths (580 and 905 nm) to calculate the apparent temperature  $T_a$ . These wavelengths were chosen as they define the endpoints of the wavelengths used in multi-wavelength two-dimensional imaging radiometry,<sup>5</sup> and are similar to the endpoints in the wavelength range for traditional temperature measurements by spectroradiometry (e.g., Refs. 2 and 3). The corresponding absorption coefficients are  $k_{580}$  and  $k_{905}$ , respectively. Assuming (1)  $k_{580}$  and  $k_{905}$  are constant throughout the sample for each wavelength, respectively; (2) the whole sample can be modeled as a simple parallel plane at  $T_m = 4000$  K (no temperature gradient exists). The  $\Delta T_a$ , deviations of apparent temperatures from apparent temperature when both optical thicknesses  $\tau_{580}$  and  $\tau_{905}$  are equal to 1 are plotted in the optical thickness space (Fig. 4). In this way, we can preclude the deviations introduced by the Wien approximation. Since increasing  $\tau_{580}$  and  $\tau_{905}$  changes the slope of Wien vs. the wavenumber plot oppositely, deviations are divided into two domains of opposite signs: the upper left-hand side of the plot shows positive  $\Delta T_a$ , while the lower right-hand side of the plot shows negative  $\Delta T_a$ . Pronounced temperature deviation occurs if  $\tau_{580} \neq \tau_{905}$  and either  $\tau_{580}$  and  $\tau_{905}$  is less than  $\sim 2$ . Differences between  $\tau_{580}$  and  $\tau_{905}$  dominate the deviation values. When either of the optical thicknesses is large enough to make  $I_\lambda(d) = E_\lambda$ , the deviations flatten out. When both  $\tau_{580}$  and  $\tau_{905}$  are greater than  $\sim 2$ , the temperature deviation is smaller than the typical system error introduced by the laser heated system ( $\sim 7\%$ ).<sup>5</sup> This is because  $I_\lambda(d) = E_\lambda$  for both wavelengths. Additionally, the  $-7\% < \Delta T_a/T_m < 7\%$  regime shrinks as  $T_m$  increases from 3000 K to 5000 K.

Previous studies suggest that most Earth mantle minerals under corresponding pressures, [e.g.,  $(\text{Mg}_{0.9}, \text{Fe}_{0.1})_2\text{SiO}_4$  olivine under upper mantle pressures,  $(\text{Mg}_{0.9}, \text{Fe}_{0.1})_2\text{SiO}_4$  wadsleyite and ringwoodite under transition zone pressures,  $(\text{Mg}_{0.9}, \text{Fe}_{0.1})\text{SiO}_3$  bridgmanite under lower mantle pressures] have relatively small absorption coefficients ( $< 1000 \text{ cm}^{-1}$ ) in 600 nm to 900 nm range.<sup>26–28</sup> For a typical LHDAC experiment, sample thickness is  $\sim 20 \mu\text{m}$  or less if pressure media are used and is pressure dependent. Therefore the corresponding optical thickness ( $\tau \approx 2$ ) falls into the regime where temperature deviation could be very large (bottom right panel of Fig. 4). Although  $(\text{Mg}_{0.9}, \text{Fe}_{0.1})\text{O}$  ferropericlase has relatively larger absorption coefficient values ( $\sim 1000 \text{ s cm}^{-1}$ ) in 600 nm to 900 nm at lower mantle pressure, its absorption coefficients are highly wavelength-dependent.<sup>27,29–31</sup> Thus the correction for wavelength-dependent absorption for LHDAC experiment of  $(\text{Mg}_{0.9}, \text{Fe}_{0.1})\text{O}$  ferropericlase is important. It is worth noting that metals usually have large absorption coefficients ( $> 10^5 \text{ cm}^{-1}$ ) in the visible to near infrared range, however the surface properties of the metal could be very different from the interior depending on factors like roughness and reflectivity. The solution to Eq. (2) for parallel planes with transparent boundaries, namely, Eq. (4), is based on the assumption that the surface optical properties are exactly the same as the materials beneath it; therefore transparent boundaries may not be an appropriate assumption for LHDAC experiments with metals.

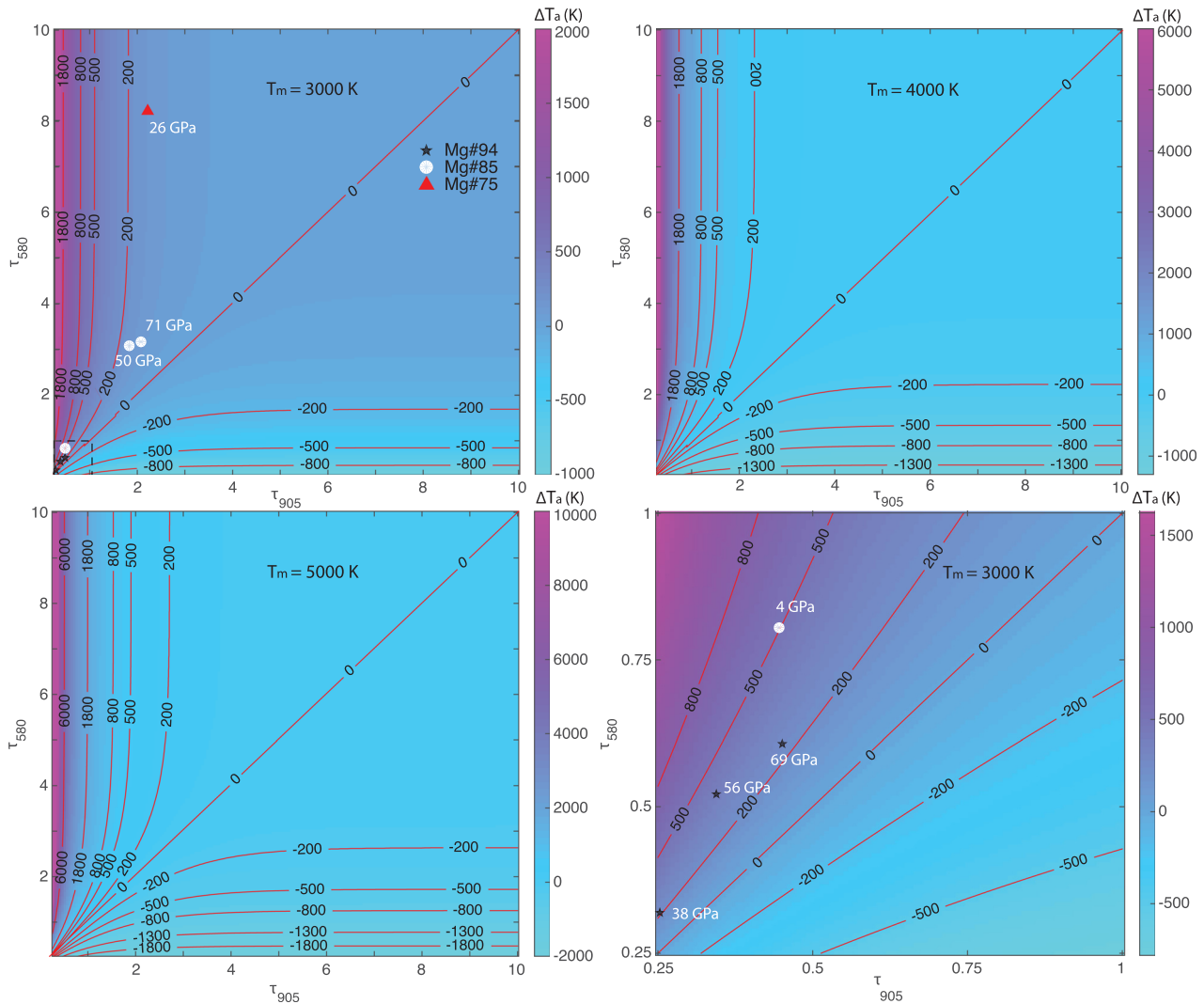


FIG. 4.  $\Delta T_a$  calculated from two-color (i.e., 580 and 905 nm) is plotted in optical thickness space at  $T_m = 3000$  K, 4000 K, and 5000 K. Dashed box in the upper left panel is shown in the bottom right panel. Optical thicknesses for ferropericlaase with different chemical compositions under various pressures are plotted assuming a sample thickness of 10  $\mu\text{m}$ .

## D. Effects of wavelength-dependent absorption and temperature gradient

### 1. Single absorption model (the entire sample has one set of wavelength-dependent absorption coefficients)

As a case study, we modeled the apparent temperatures for the sample configuration shown in Fig. 3(a). Two cases were considered: (1) the absorption coefficients,  $k_1$  (therefore  $\tau_1$ ) linearly increase with wavelength (Fig. 5(a)); (2) the absorption coefficients,  $k_2$  ( $\tau_2$ ) linearly decrease with wavelength (Fig. 5(c)). These linear increase and decrease trends are simplifications for absorption spectra that could occur in the near infrared (NIR) to ultraviolet (UV) range, where multiple absorption mechanisms exist. Taking (Mg, Fe)O as an example, the absorption edge related to charge transfer d-d transitions between adjacent  $\text{Fe}^{2+}$  sites or charge transfer between Fe-O usually dominate the shape of absorption spectra and cause a linear increase in absorption coefficients with a wavenumber in the visible and UV range.<sup>29</sup> However, this absorption edge shows a “blue shift” with the decrease of pressure. As such, absorption coefficients can decrease

with wavenumber if a sample is under relatively low pressure and also mechanisms corresponding to the absorption peaks at smaller wavenumber (e.g., Jahn-Teller effects can split absorption bands and consequently induce an absorption peak at around  $10000\text{ cm}^{-1}$ ) dominate the shape of absorption spectra.<sup>30,31</sup> Apart from these simple decrease and increase trends, more complicated relationships between absorption coefficients and wavenumber can occur if peaks corresponding to the spin transition of  $\text{Fe}^{2+}$  or  $\text{Fe}^{3+}$  dominate the spectra. Here we only consider the decrease and increase trends to simplify. Additionally, absorption coefficients are increased or decreased by a factor of five to show the influence of the absolute value of optical thicknesses on apparent temperature deviation. These types of variation of absorption coefficients in the NIR to UV range can be caused by the iron abundance or change in pressure.<sup>29</sup>

Horizontal apparent temperature profiles corresponding to these six cases when  $T_m = 4000$  K are displayed in Figs. 5(b) and 5(d).  $T_a$  profile when the optical thicknesses are 1 for 580, 640, 766, and 905 nm (i.e.,  $T_{grad}$ ) is also presented in order to compare the horizontal apparent temperature

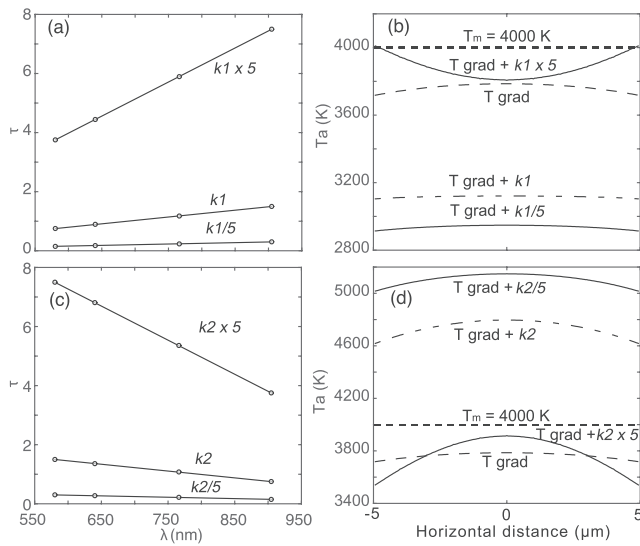


FIG. 5. Optical thicknesses of the sample and the corresponding horizontal  $T_a$  profile across the center of the sample calculated by single absorption model when  $T_m = 4000$  K. (a) Optical thickness that increases with wavelength,  $k1$ . (b) Corresponding apparent temperature  $T_a$  profiles measured assuming only the axial temperature gradients ( $T grad$ ) and with various optical thicknesses. For example,  $T grad + k1$  corresponds to the scenario where axial temperature gradients are present in the sample, and the absorption coefficient of the whole sample is  $k1$ . (c) Optical thickness that decreases with the wavelength,  $k2$ . (d) Corresponding apparent temperature  $T_a$  profiles measured assuming axial temperature gradients ( $T grad$ ) and various optical thicknesses.

profile caused solely by the axial temperature gradient and that caused by the axial temperature gradient and wavelength dependent absorption together. Note that the absolute value of the apparent temperatures for the case when no wavelength-dependent absorption and temperature gradients are present (i.e.,  $T grad$ ) changes with the values of absorption coefficients. When  $\tau_{580}$  and  $\tau_{905}$  are equal and very large, all the horizontal apparent temperatures will be very close to the diamond-sample interface temperature, i.e., 300 K. As such, what matters is the shape of the horizontal  $T_a$  profile for the wavelength independent absorption case. Additionally, as pointed out above, it always shows a convex parabolic shape with the highest  $T_a$  in the center of the sample. In contrast, the  $T_a$  profiles for wavelength dependent absorption case is more varied (Fig. 5(b,d)): it can be a convex parabolic shape with the highest  $T_a$  in the center of the sample, or somewhat flat ( $T grad + k1$ ,  $T grad + k1/5$ ), or a concave parabolic shape with the highest  $T_a$  at the ends ( $T grad + k1 \times 5$ ).

The general trend is that temperature gradients always lower the peak temperature whereas the existence of wavelength dependent absorption could either underestimate or overestimate the peak temperature depending on whether low energy (long wavelength) radiation signals or high energy (short wavelength) radiation signals are relatively enhanced. For example, for the case shown in Fig. 5(a),  $E_{\lambda=905 \text{ nm}}$  exiting each layer is relatively enhanced when  $k_{\lambda=905 \text{ nm}}$  is largest. But it should be noted that once the  $E_{\lambda=905 \text{ nm}}$  is emitted out of each layer, it also gets absorbed by other layers the most because here we assume all the layers have the same  $k_{\lambda}$ . Overall,  $T grad + k1 \times 5$ ,  $T grad + k1$  and  $T grad + k1/5$  yield apparent temperatures

smaller than 4000 K since the corresponding optical thickness decrease with wavenumber whereas  $T_a$  for  $T grad + k2$  and  $T grad + k2/5$  are much larger than 4000 K. It is also interesting to note that (1)  $T_a$  for  $T grad + k1 \times 5$  and  $T grad + k2 \times 5$  could be quite close to the real peak temperature, 4000 K; (2)  $T_a$  for the two ends of  $T grad + k1 \times 5$  is even larger than 4000 K and  $T_a$  for  $T grad + k2 \times 5$  is smaller than 4000 K. Both (1) and (2) are caused by the absorption effects of the “cold” layer above the “hot” layer (e.g., melt).  $T grad + k1 \times 5$  and  $T grad + k2 \times 5$  are characterized by large overall absorption coefficients. At the two ends of  $T grad + k1 \times 5$ , the cold solid is thick enough that its absorption effects dominate and therefore relatively undermine the  $E_{\lambda=905 \text{ nm}}$ , yielding  $T_a$  larger than 4000 K. Similarly, for  $T grad + k2 \times 5$ , absorption effects of the cold solid always dominate while at the center, the absorption of the cold solid is weaker since there is less solid there. Consequently, the  $T_a$  for  $T grad + k2 \times 5$  is maximum in the center and decreases away from the center.

To conclude, the interaction between temperature gradients and wavelength-dependent absorption/emission can result in various types of  $T_a$  profiles. A flattened  $T_a$  profile does not necessarily mean that the temperature measurement is accurate, although desirable. In the case shown in  $T grad + k1/5$ ,  $T_a$  is fairly flat across the sample but it is indeed more than 1000 K lower than the  $T_m$  (Fig. 5(b)). In addition, melting curves of semi-transparent materials may need to be re-visited and the effects of wavelength-dependent absorption need to be corrected. We also predict that various shapes of the horizontal  $T_a$  profiles could occur besides the flat, concave, or convex shape depending on the sample configuration and its optical properties.

## 2. Multi-layer absorption model (each layer has a different set of wavelength-dependent absorption coefficients)

The single-absorption model requires that the whole sample maintains the same absorption coefficients during laser heating. This is hard to achieve and somewhat unrealistic especially for an iron-containing sample where Soret diffusion is common. Additionally, iron generally prefers the melt and consequently the absorption coefficients of melts will be much larger than its surrounding iron-depleted co-existing solid and starting materials (e.g., Refs. 7 and 8). Even if melting does not occur during laser heating, chemical differentiation or phase transformations may occur, yielding layers of different absorption characteristics.

Here we consider a simplified case when the starting material is annealed from one side and then the laser heated from the same side, assuming the same sample configuration as Fig. 3(a). Solids on the heated side are assumed to have the same absorption coefficient,  $k_{\text{annealed}} = k1/5$ ; the melt is enriched in iron and thus has a higher absorption value  $k_{\text{melt}} = k1 \times 5$ ; and the solids on the unheated side are unannealed and have  $k_{\text{unannealed}} = k1$  as in Fig. 6(c) ( $k2$  in Fig. 6(e)). We denote the absorption coefficient combination as ( $k1/5 : k1 \times 5 : k1$ ) or ( $k2/5 : k2 \times 5 : k2$ ). Note that the optical thickness of each layer is different from the values shown in Fig. 5

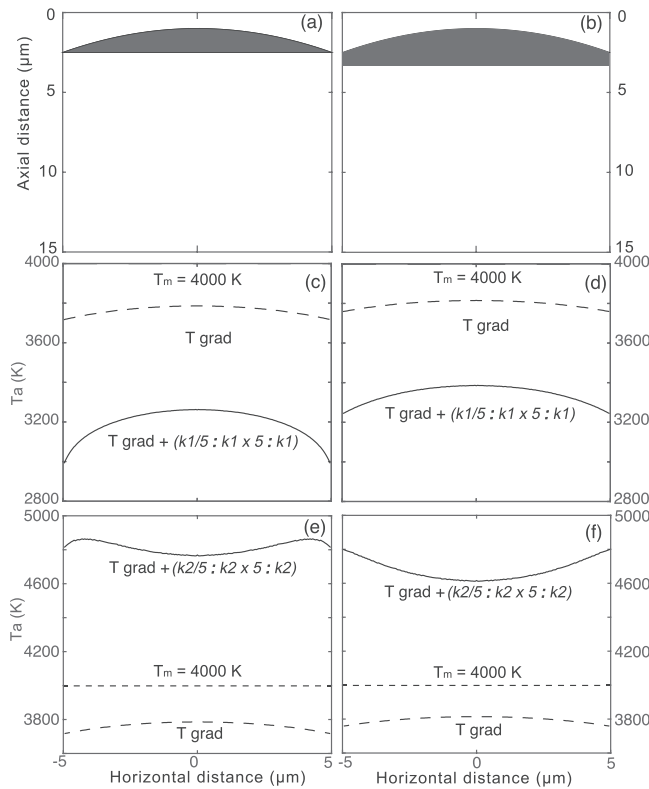


FIG. 6. Horizontal  $T_a$  profile across the center of the sample calculated by the multi-layer absorption model when  $T_m = 4000$  K. (a) and (b) represent the sample configuration used in the three-layer model. (c) and (e) correspond to the sample configuration shown in (a). (d) and (f) correspond to the sample configuration if  $1 \mu\text{m}$  of additional melt is added to the sample configuration as shown in (b).

because the thickness of each layer is less than  $15 \mu\text{m}$ . Therefore,  $T \text{ grad} + (k1/5 : k1 \times 5 : k1)$  represents that axial temperature gradients are present in the sample and the absorption coefficients of the annealed, melt and unannealed layers are  $k1/5, k1 \times 5, k1$ , respectively.  $T \text{ grad} + (k1/5 : k1 \times 5 : k1)$  yields in overall much smaller  $T_a$  values across the center part of the sample than those given by  $T \text{ grad} + (k2/5 : k2 \times 5 : k2)$  as expected assuming  $T_m = 4000$  K. In terms of the shape of the  $T_a$  profiles,  $T \text{ grad} + (k1/5 : k1 \times 5 : k1)$  shows a convex parabola whereas  $T \text{ grad} + (k2/5 : k2 \times 5 : k2)$  shows a concave shape where  $T_a$  in the center is slightly smaller than the nearby surroundings. If  $1 \mu\text{m}$  of melt is added into the sample configuration in Fig. 6(a) and the other parameters are kept the same (Fig. 6(b)),  $T \text{ grad} + (k1/5 : k1 \times 5 : k1)$  still shows a convex parabola whereas  $T \text{ grad} + (k2/5 : k2 \times 5 : k2)$  shows a concave parabola (Figs. 6(d) and 6(f)). Figs. 6(e) and 6(f) can potentially explain the  $T_a$  offset in the 2D temperature map of sample May2915 (Fig. 2(i)).

Although our discussion is limited to a simple three-layer model for melting experiments, it can be easily extrapolated to a more complicated N-layer model for any type of LHDAC experiments even if melt is not present as long as the temperature profile and absorption properties of materials are well constrained.

It is also worth discussing the cases when common thermal insulators (e.g., NaCl, KCl, Ar, etc.) are used. The commonly used thermal insulators are generally characterized by

small and wavelength-independent absorption coefficients in 580, 640, 766, and 905 nm. Therefore, although the large temperature gradients can be present within thermal insulators and usually they are as thick as the sample, they neither emit radiation nor absorb the radiation from the sample at 580, 640, 766, and 905 nm at least at relatively low pressures and temperatures ( $<100$  GPa,  $<1000$  s of K (Ref. 32)). In other words, they do not participate in the optical processes in that wavelength range. If a sample is isothermal, the effects of wavelength-dependent absorption of the whole sample assemblage are the same as those shown in Fig. 4. As such, the thermal insulators are useful to keep the intensity of thermal radiation of the sample unchanged and thus yield more accurate temperature measurements. However, thermal insulators may contaminate the sample especially when the sample is melted.<sup>7</sup> In addition, sometimes samples are still thermally layered even with thermal insulators (see Fig. S1 in Ref. 33). Indeed, all of the above factors need to be carefully considered when designing LHDAC experiments.

## V. INVERSE MODELING

In LHDAC experiments, we collect the intensities of light by CCD, based on which,  $T_a$  can be calculated. As discussed above, the  $T_a$  could be quite off from the actual highest temperature ( $T_m$ ) during laser heating because of

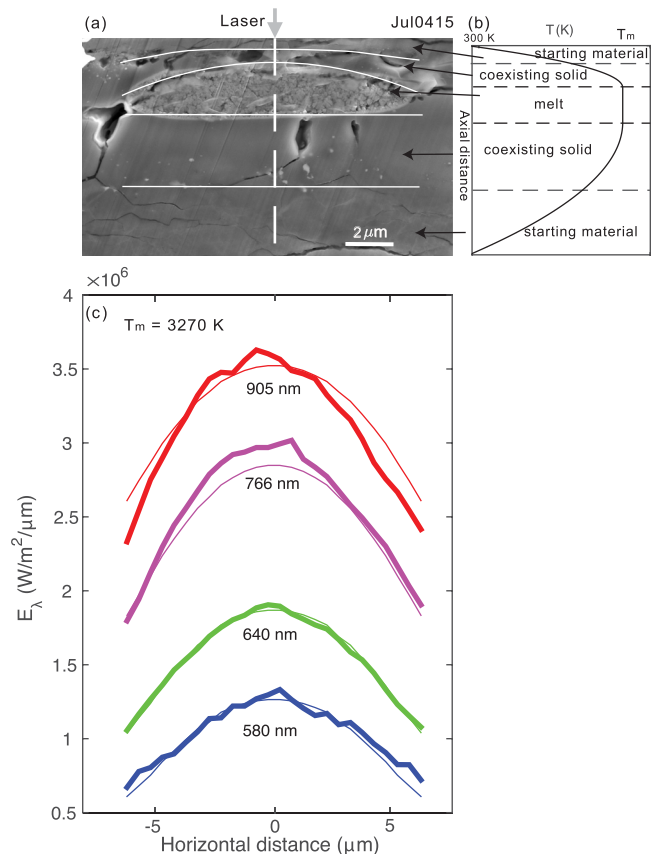


FIG. 7. (a) Scanning electron microscope image of the cross section of the sample Jul0415. (b) Schematic of the five layers (corresponding to the layers divided by white solid lines in (a) and the axial temperature. (c) Corresponding inverse modeling results. The thick lines are the horizontal intensities of radiation detected, and the thin lines are the fitted results with the corresponding wavelength labeled.

temperature gradients and wavelength-dependent absorption. Here we propose an inverse modeling method based on the FIB cross-sections (Fig. 7(a)) of the sample and the thermal radiation intensity profile (horizontal intensity profiles in four wavelengths from the multi-wavelength two-dimensional imaging radiometry or continuous intensity profile from a single point for spectroradiometric approaches) to rigorously constrain the actual highest temperature.

An example of inverse modeling for 4-color multi-wavelength two-dimensional temperature mapping is shown in Fig. 7. In order to determine  $T_m$ , we analyzed the data in the following manner:

- (1) Find the horizontal intensity profiles for each of the four wavelengths based on the orientation of the cross section and optical images (three white dashed lines in Figs. 2(a), 2(d), and 2(g)). Note, the horizontal intensity profiles used in the inverse modeling only extends to the boundary between coexisting solid and melt (or hottest part if melt is absent) as shown by white lines in Fig. 7(a) in order to obtain data with high a signal-to-noise ratio. The boundary between the coexisting solid and starting material is somewhat blurry, which may introduce some errors.
- (2) Construct the temperature profile. Here we use the axial temperature profiles obtained by solving Eq. (1) (Fig. 7(b)). As can be seen in Fig. 7(b), we divide the sample along the axial direction into five layers. They are as follows: starting material, coexisting solid, melt, coexisting solid, and starting material in order from top to bottom. More rigorous temperature profiles can be calculated using the TempDAC code<sup>10</sup> with the knowledge of thermodynamic properties of materials at corresponding conditions. But unfortunately, those parameters are poorly constrained for most Earth materials at elevated pressures and temperatures. Nevertheless, the fine structure of the temperature profile obtained by rigorous thermodynamic simulation is not expected to change the axial temperature distribution within the melt (hot part) much while it does alter the fine structure of the temperature profile of the solid part (cold part). As such, temperature correction will not be influenced largely ( $\sim 4\%$  estimated for Fig. 7 top panel in Ref. 10) by the rigorous temperature profile calculation since the hottest part dominates the effects of the temperature gradient as discussed above. Additionally, we use a parabolic shape to approximate the melt-coexisting solid boundary on the heated side for Jul0415 (Fig. 7(a)) because a simple parabola is sufficient to describe the boundary.
- (3) Following the same procedure in the forward modeling, we search for a  $T_m$ , which minimizes the misfit value that is computed using a normalized residual sum of squares (RSS):

$$RSS = \frac{1}{N} \sum_{q=1}^4 \sum_{i=1}^n \left( \frac{I_{i,\lambda_q}^{\text{predict}} - I_{i,\lambda_q}^{\text{CCD}}}{I_{i,\lambda_q}^{\text{predict}}} \right)^2, \quad (7)$$

where  $I_{i,\lambda_q}^{\text{predict}}$  ( $I_{i,\lambda_q}^{\text{CCD}}$ ) is the calculated (CCD detected after system response correction) intensity of radiation at

position  $i$  of wavelength  $\lambda_q$ ,  $N = 4n$  is the total number of intensity points used to do the inverse modeling, and  $n$  is the number of intensity points at each wavelength. Using the available literature data,<sup>22,27,29</sup> sample absorption coefficients are interpolated for  $Mg\# \geq 75$  and extrapolated for  $Mg\# < 75$  (see [supplementary material](#)).

The fitting result for sample Jul0415 is shown in Fig. 7. The best fitting horizontal intensity of radiation curves (thin lines in Fig. 7(d)) are generally very consistent with the detected data (thick lines) except that the fitted results are overall slightly higher than the detected values. This may be due to inaccurate interpolation or extrapolation of the absorption coefficients at a particular wavelength. Besides, the fitted curves become increasingly off from the real data at the ends. This is reasonable since the white lines in Fig. 7(a) do not delineate the layer boundaries at the two ends very well.

Inverse modeling results for samples May2715C and May2915 do not include the thermal radiation at 580 nm as the modeled intensities do not fit the detected intensities of light at this wavelength. This is likely due to the large variability (up to a factor of four) of absorption coefficients of ferropericlase at 580 nm with a slight change in  $Fe^{3+}$  concentrations<sup>30</sup> (see [supplementary material](#) for the fitting results of these two samples). The results of  $T_m$  for all the samples in this study are summarized in Table I. The uncertainties of  $T_m$  obtained through this method are given by the temperatures that yield normalized RSSs which are within the 95% confidence range of minimum normalized RSS. Those uncertainties are generally quite small ( $< 1\%$ ) since normalized RSSs changes sharply away from the best fitting  $T_m$ . For example, the  $T_m$  range corresponding to the 95% confidence range of minimum normalized RSS for Jul0415 is 3240 K to 3300 K (see [supplementary material](#)). Besides the uncertainties of this method, as discussed in Ref. 5, other factors such as calibrations and corrections, resolution of melt bleb texture and corresponding temperature map will contribute an additional  $\sim 3\%$  in uncertainties. Additionally, the spatial resolution of the CCD camera measuring the hot spot is finite and determined by the resolving limit of the optics and will cause the light emanating from one spot to be averaged with surrounding spots. We have measured the spatial resolution of our multi-wavelength two-dimensional imaging radiometry<sup>4,5</sup> system to be  $5 \mu\text{m}$  at 640 nm, similar to that found in a similar setup:  $4 \mu\text{m}$  at 670 nm.<sup>4</sup> As shown by Campbell,<sup>4</sup> this resolving limit causes modest artifacts in the temperature measurement ( $\sim 2\%$ ). Thus, the uncertainty for our inverse modeling in Table I ( $\sim 10\%$ ) is the combined value including all of the factors above. In addition, an averaged temperature along the loop (Figs. 2(c), 2(f), and 2(i)) encompassing Region I in the 2-D temperature maps<sup>5</sup> (denoted as perimeter temperature in Table I) and  $T_a$  of the hottest point are also listed in Table I. The index (or position) of the hottest point is searched by minimizing  $\sum_{q=1}^4 (I_{\text{index},\lambda_q}^{\text{CCD}} - \max(I_{\lambda_q}^{\text{CCD}}))^2$ , where  $\max(I_{\lambda_q}^{\text{CCD}})$  is the maximum intensity value at wavelength  $\lambda_q$ . The hottest point is usually located in the center of the melt spot. The difference between  $T_m$  given by the inverse modeling and highest temperature given by the other two methods is as large as  $\sim 700$  K for these three samples.

TABLE I. Summary of experimental conditions and results. Compositions are measured for the quenched samples after laser heating. Uncertainties of pressures and compositions are given in parentheses. Temperature uncertainties are  $\sim 7\%$  for perimeter and hottest point values and is  $\sim 10\%$  for inverse modeling ( $T_m$ ). The perimeter temperature corresponds to the apparent temperature calculated by averaging the temperatures along the loop (Figs. 2(c), 2(f), and 2(i)) encompassing Region I in 2-D temperature maps<sup>5</sup> and the hottest point is searched by minimizing  $\sum_{q=1}^4 (I_{index, \lambda_q}^{CCD} - \max(I_{\lambda_q}^{CCD}))^2$ , where  $\max(I_{\lambda_q}^{CCD})$  is the maximum intensity value at wavelength  $\lambda_q$ .

Run#	P (GPa)	Starting material (Mg#)	Melt (Mg#)	Coexisting solid (Mg#)	Temperature (K)		
					Perimeter, $T_a$	Hottest point, $T_a$	Inverse modeling, $T_m$
May2715C	51(1)	88(1)	71(1)	91(1)	4250	4500	3800 <sup>a</sup>
Jul0415	60(1)	81(1)	59(1)	90(1)	2600	2750	3270
May2915	66(1)	88(1)	67(5) <sup>b</sup>	98(5) <sup>b</sup>	4200	4350	3650 <sup>a</sup>

<sup>a</sup>Three-color (640, 766, and 905 nm) temperature fit.

<sup>b</sup>Results are from semi-quantitative analysis by Energy Dispersive Spectroscopy (EDS).

In the case of a spectroradiometric temperature measurement and single point radiation intensity detection, all the procedures are the same except that the normalized  $RSS$  is defined by

$$RSS = \frac{1}{N} \sum_{q=1}^N \left( \frac{I_{\lambda_q}^{predict} - I_{\lambda_q}^{CCD}}{I_{\lambda_q}^{predict}} \right)^2, \quad (8)$$

where  $q$  is the number of wavelengths of radiation detected by spectrometry after the system response correction, and the other terms follow the same meaning in Eq. (7).

There are other possible sources of error that we have not included in our model. The largest source of uncertainty stems from the absorption values used for each layer as the absorption properties of materials are controlled and complicated by a lot of different factors as discussed in Section IV.<sup>27,29,34,35</sup> The darker the material (either due to composition or increased pressure), the harder it is to make absorption measurements, as such, the data in the literature is limited and so extrapolation was necessary (see [supplementary material](#)).

## VI. CONCLUSIONS

In this study, using ferropericlase as an example, we demonstrate that temperature gradients and wavelength-dependent absorption coefficients of starting materials can drastically deviate from the apparent temperature measured in a LHDAC experiment from the real highest temperature reached during the experiment.

The effects of temperature gradients on temperature determination can be accounted for with the knowledge of the temperature profiles of a sample. In contrast, correction for wavelength-dependent absorption/emission requires the absorption spectra of materials under various pressures and temperatures, which are difficult to obtain and for many materials poorly studied. If the materials are opaque, and the surface emissivity is weakly wavelength dependent in the NIR and visible range (e.g., FeO, Fe, Pt, and most other metals), the materials can be fairly treated as a blackbody and the correction for wavelength-dependent absorption/emission is unnecessary. However, it is widely acknowledged that materials which contain the transition metals usually have absorption peaks in the visible light range

because of the spin-allowed d-d transitions and intervalence charge transfer (IVCT) and the splitting of absorption bands at this wavelength range could be caused by Jahn-Teller effects.<sup>35</sup> The amplitude and position of absorption peaks are functions of chemical composition, grain size, and physical conditions. For semi-transparent materials, strongly wavelength-dependent absorptions are likely to be present in the wavelengths that are also used to measure temperatures in LHDAC experiments. Because the melting temperatures of such materials are of great significance in planetary (e.g., ferropericlase, (Mg, Fe)SiO<sub>3</sub> bridgmanite) and material (e.g., SiC, TiO<sub>2</sub>) sciences, a careful examination of the wavelength-dependent absorption on temperature determination in previous LHDAC experiments (e.g., Refs. 3, 7, 8, 33, and 36–38) is therefore necessary.

## SUPPLEMENTARY MATERIAL

See [supplementary material](#) for the interpolation and extrapolation of absorption coefficients and normalized  $RSS$  for the fitting of sample Jul0415. Inverse modeling results for samples May2915 and May2715C are also shown.

## ACKNOWLEDGMENTS

We would like to thank Ronald Smith, Yohsinori Miyazaki, Sergey Lobanov, and Alexander Goncharov for helpful discussions. We are grateful to two anonymous reviewers for very useful comments and suggestions that improved the paper. Z. Du thanks Carnegie Postdoctoral Fellowship for financial support. This work was supported by NSF (EAR-1321956, EAR-1551348). FIB use was supported by YINQE and NSF MRSEC DMR 1119826 and by the Center for Functional Nanomaterials, Brookhaven National Laboratory, which is supported by the U.S. Department of Energy, Office of Basic Energy Sciences. Prepared by LLNL under Contract Nos. DE-AC52-07NA27344 and LLNL-JRNL-706083.

<sup>1</sup>R. Jeanloz, A. Kavner, P. Lazor, and S. K. Saxena, *Philos. Trans.: Math., Phys. Eng. Sci.* **354**, 1279 (1996).

<sup>2</sup>Y. Meng, R. Hrubiak, E. Rod, R. Boehler, and G. Y. Shen, *Rev. Sci. Instrum.* **86**, 072201 (2015).

<sup>3</sup>R. Nomura, K. Hirose, K. Uesugi, Y. Ohishi, A. Tsuchiyama, A. Miyake, and Y. Ueno, *Science* **343**, 522 (2014).

<sup>4</sup>A. J. Campbell, *Rev. Sci. Instrum.* **79**, 015108 (2008).

- <sup>5</sup>Z. Du, G. Amulele, L. R. Benedetti, and K. K. M. Lee, *Rev. Sci. Instrum.* **84**, 075111 (2013).
- <sup>6</sup>L. R. Benedetti, N. Guignot, and D. L. Farber, *J. Appl. Phys.* **101**, 013109 (2007).
- <sup>7</sup>Z. Du and K. K. M. Lee, *Geophys. Res. Lett.* **41**, 8061, doi:10.1002/2014GL061954 (2014).
- <sup>8</sup>R. Nomura, H. Ozawa, S. Tateno, K. Hirose, J. Hernlund, S. Muto, H. Ishii, and N. Hiraoka, *Nature* **473**, 199 (2011).
- <sup>9</sup>D. L. Heinz and R. Jeanloz, in *High-Pressure Research in Mineral Physics: A Volume in Honor of Syun-iti Akimoto* (American Geophysical Union, 1987), p. 113.
- <sup>10</sup>E. S. G. Rainey, J. W. Hernlund, and A. Kavner, *J. Appl. Phys.* **114**, 204905 (2013).
- <sup>11</sup>L. R. Benedetti and P. Loubeyre, *High Pressure Res.* **24**, 423 (2004).
- <sup>12</sup>A. Kavner and W. R. Panero, *Phys. Earth Planet. Inter.* **143–144**, 527 (2004).
- <sup>13</sup>G. Y. Shen, M. L. Rivers, Y. B. Wang, and S. R. Sutton, *Rev. Sci. Instrum.* **72**, 1273 (2001).
- <sup>14</sup>D. L. Heinz, J. S. Sweeney, and P. Miller, *Rev. Sci. Instrum.* **62**, 1568 (1991).
- <sup>15</sup>O. R. Burggraf, *J. Heat Transfer* **86**, 373 (1964).
- <sup>16</sup>F. H. R. Franca, O. A. Ezekoye, and J. R. Howell, *J. Heat Transfer* **123**, 884 (2001).
- <sup>17</sup>S. C. Sun, H. Qi, F. Z. Zhao, L. M. Ruan, and B. X. Li, *Appl. Therm. Eng.* **98**, 1104 (2016).
- <sup>18</sup>R. Jeanloz and D. L. Heinz, *J. Phys.* **45**, 83 (1984).
- <sup>19</sup>R. Boehler, N. Vonbargen, and A. Chopelas, *J. Geophys. Res., [Solid Earth Planets]* **95**, 21731 (1990).
- <sup>20</sup>J. S. Sweeney and D. L. Heinz, *Properties of Earth and Planetary Materials at High Pressure and Temperature* (American Geophysical Union, 1998), Vol. 101, p. 197.
- <sup>21</sup>S. Bodea and R. Jeanloz, *J. Appl. Phys.* **65**, 4688 (1989).
- <sup>22</sup>A. F. Goncharov, P. Beck, V. V. Struzhkin, B. D. Haugen, and S. D. Jacobsen, *Phys. Earth Planet. Inter.* **174**, 24 (2009).
- <sup>23</sup>A. M. Hofmeister and J. M. Branlund, in *Treatise on Geophysics*, 2nd ed., edited by G. Schubert (Elsevier, Oxford, 2015), p. 583.
- <sup>24</sup>K. Otsuka, C. A. McCammon, and S.-I. Karato, *Phys. Earth Planet. Inter.* **180**, 179 (2010).
- <sup>25</sup>H. Watanabe, M. Susa, H. Fukuyama, and K. Nagata, *Int. J. Thermophys.* **24**, 473 (2003).
- <sup>26</sup>S. M. Thomas, C. R. Bina, S. D. Jacobsen, and A. F. Goncharov, *Earth Planet. Sci. Lett.* **357–358**, 130 (2012).
- <sup>27</sup>A. F. Goncharov, B. D. Haugen, V. V. Struzhkin, P. Beck, and S. D. Jacobsen, *Nature* **456**, 231 (2008).
- <sup>28</sup>T. J. Shankland, U. Nitsan, and A. G. Duba, *J. Geophys. Res.* **84**, 1603, doi:10.1029/JB084iB04p01603 (1979).
- <sup>29</sup>A. F. Goncharov, V. V. Struzhkin, and S. D. Jacobsen, *Science* **312**, 1205 (2006).
- <sup>30</sup>A. F. Goncharov, V. V. Struzhkin, J. A. Montoya, S. Kharlamova, R. Kundargi, J. Siebert, J. Badro, D. Antonangeli, F. J. Ryerson, and W. Mao, *Phys. Earth Planet. Inter.* **180**, 148 (2010).
- <sup>31</sup>H. Keppler, I. Kantor, and L. S. Dubrovinsky, *Am. Mineral.* **92**, 433 (2007).
- <sup>32</sup>R. S. McWilliams, D. A. Dalton, Z. Konopkova, M. F. Mahmood, and A. F. Goncharov, *Proc. Natl. Acad. Sci. U.S.A.* **112**, 7925 (2015).
- <sup>33</sup>G. Fiquet, A. L. Auzende, J. Siebert, A. Corgne, H. Bureau, H. Ozawa, and G. Garbarino, *Science* **329**, 1516 (2010).
- <sup>34</sup>S. S. Lobanov, N. Holtgrewe, and A. F. Goncharov, *Earth Planet. Sci. Lett.* **449**, 20 (2016).
- <sup>35</sup>R. G. Burns, *Mineralogical Applications of Crystal Field Theory*, 2nd ed. (Cambridge University Press, Cambridge, England, New York, NY, USA, 1993).
- <sup>36</sup>G. K. Pradhan, G. Fiquet, J. Siebert, A. L. Auzende, G. Morard, D. Antonangeli, and G. Garbarino, *Earth Planet. Sci. Lett.* **431**, 247 (2015).
- <sup>37</sup>A. Zerr and R. Boehler, *Science* **262**, 553 (1993).
- <sup>38</sup>J. S. Sweeney and D. L. Heinz, *Geophys. Res. Lett.* **20**, 855, doi:10.1029/93GL00556 (1993).

## SUPPLEMENTARY MATERIAL

### Absorption coefficients

In order to interpolate (for  $Mg\# \geq 75$ , where  $Mg\# = 100 \times Mg/(Mg+Fe)$ ) or extrapolate ( $Mg\# < 75$ ) absorption coefficient values to use in the inverse modeling, we found reported values for ferropericlasite at pressures nearest to our pressure conditions (Tables S1, S2). To supplement the absorption data in the literature, for both sets of high-pressure values, we assumed the optical absorption coefficient is 0 when  $Mg\# = 100$  (i.e., pure MgO). We then fit the absorption coefficient values<sup>1-3</sup> to a cubic polynomial for the 580, 640, 766 nm wavelengths. For the 905 nm wavelength, the absorption coefficients become negative at high  $Mg\#$  if fit to a cubic polynomial. Therefore we used a quadratic polynomial to fit the reported absorption data for 905 nm instead. All the fitted results are shown in FIG. S1.

**TABLE S1.** Previously reported optical absorption data used to interpolate and extrapolate the absorption coefficient values of (Mg, Fe)O with various compositions for samples May2715C and Jul0415, which were at pressures of 51 and 60 GPa, respectively.

Wavelength (nm)	580	640	766	905	Ref
Absorption coefficient ( $cm^{-1}$ )	15000	12000	6700	3700	Mg#75, 55 GPa <sup>1</sup>
	3050	2450	2300	1800	Mg#85, 50 GPa <sup>2,3</sup>
	520	520	480	350	Mg#94, 56 GPa <sup>1</sup>

**TABLE S2.** Previously reported optical absorption data used to interpolate and extrapolate the absorption coefficient values of (Mg, Fe)O with various compositions for sample May2915, held at 66 GPa.

Wavelength (nm)	580	640	766	905	Ref
Absorption coefficient ( $cm^{-1}$ )	15050	12050	6800	3800	Mg#75, 65 GPa <sup>1</sup>
	3150	3050	2500	2050	Mg#85, 71 GPa <sup>2</sup>

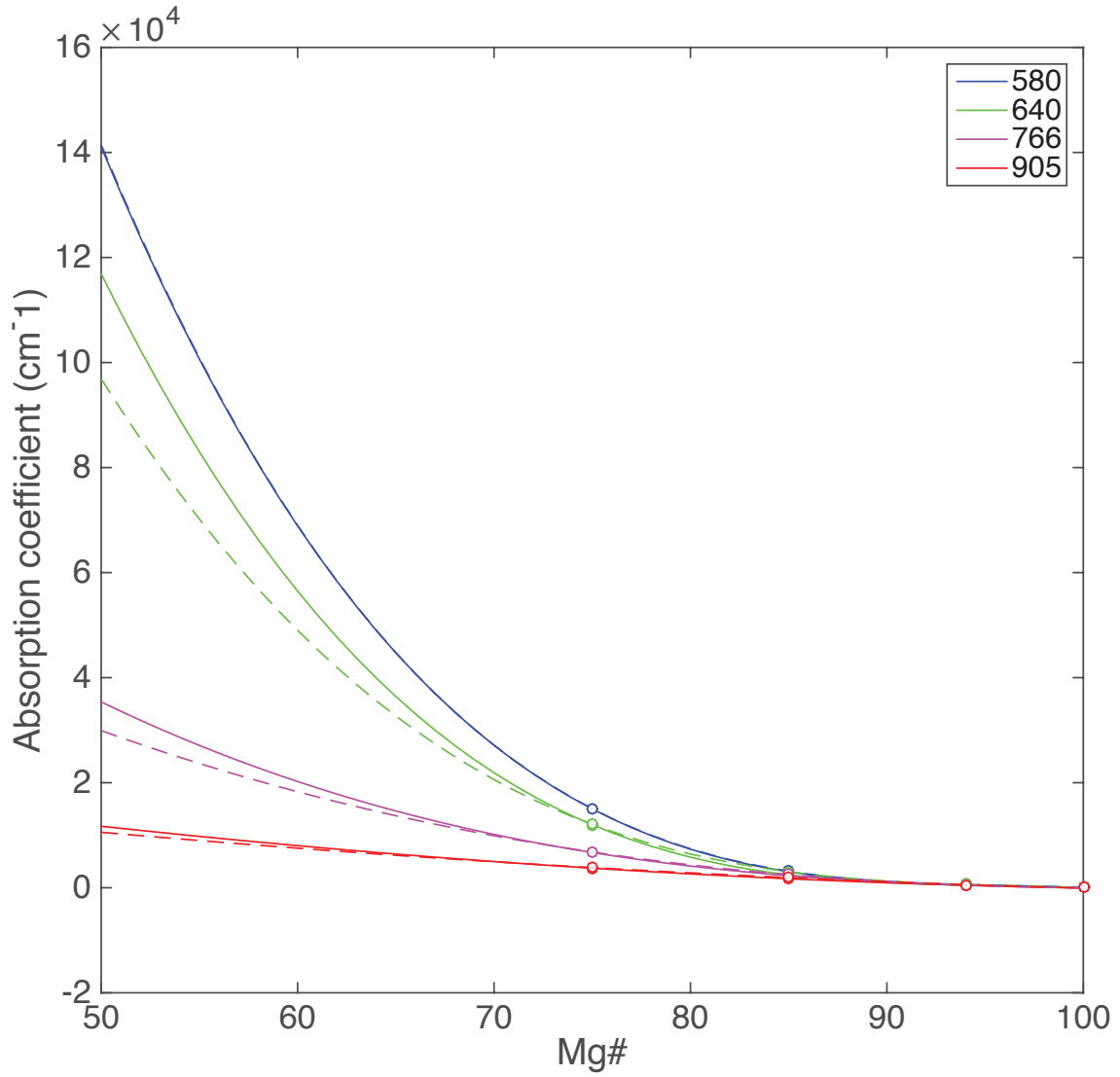


**FIG. S1.** Extrapolated ( $Mg\# < 75$ ) and interpolated ( $Mg\# \geq 75$ ) optical absorption coefficients vs.  $Mg\#$  for (Mg, Fe)O at 580, 640, 766, 905 nm to  $Mg\# = 50$ . Dashed (solid) lines correspond to values listed in Table S1 (S2).

**95% confidence range of minimum normalized residual sum of squares (RSS)**

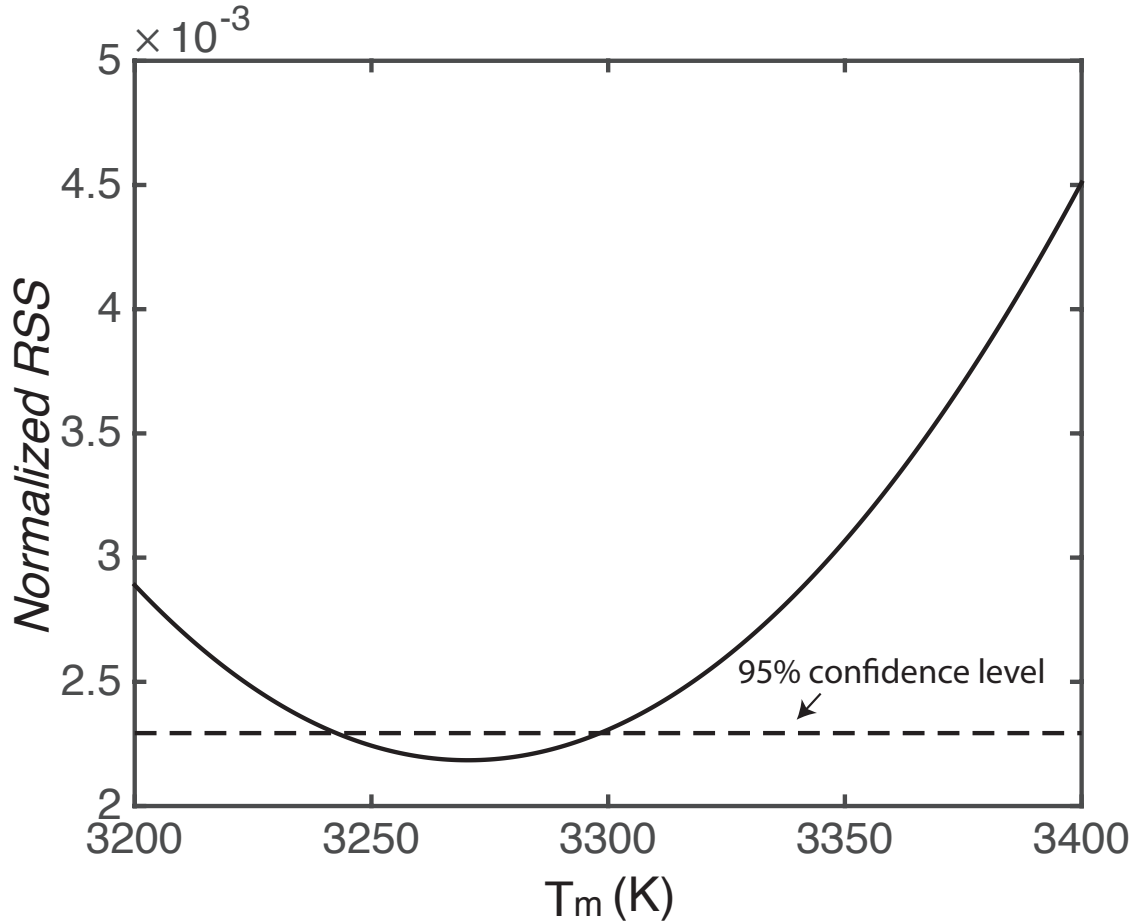


**FIG. S2.** Normalized  $RSS$  vs.  $T_m$  (melting temperature) in inverse modeling for sample Jul0415 showing minimum  $RSS$  at  $T_m = 3270$  K. The  $T_m$  range within the 95% confidence level is very narrow (3240 – 3300 K)

### Inverse modeling results for samples May2715C and May2915

Using the absorption coefficients shown in the Fig. S1, the modeled thermal radiation at 580 nm does not adequately fit detected thermal radiations for samples May2715C and May2915. This is likely because absorption coefficients of ferropicrlase at 580 nm are subject to a much larger variation (up to a factor of four at  $\sim 40$  GPa) due to small variations in  $Fe^{3+}$  concentration compared with the absorption coefficients at 640, 766, 905  $nm^4$ . Therefore, we did not include 580 nm when doing the inverse modeling of these two samples.

Additionally, for sample May2715C (Fig. S3), a large void space as well as many cracks are visible likely due to decompression, thus the geometry of the sample was modified after heating. Although this late modification was taken into account when we fit the intensity profile, it may inevitably introduce some errors to the fitting results. For sample May2915 (Fig. S4), the sample geometry is better preserved although some decompression cracks are also present. Overall, the modeled radiation intensities at 640, 766 and 905 nm fit the detected intensities well.

While having more colors to determine a temperature are preferred, the three-color fitting does not decrease our fitting accuracy since we still have a lot of data to fit the melting temperature. For example, there are 30 thermal radiation intensity values for sample May2915 at each wavelength. This means we are using 90 (rather than 120) intensity data to fit the one unknown parameter,  $T_m$ .

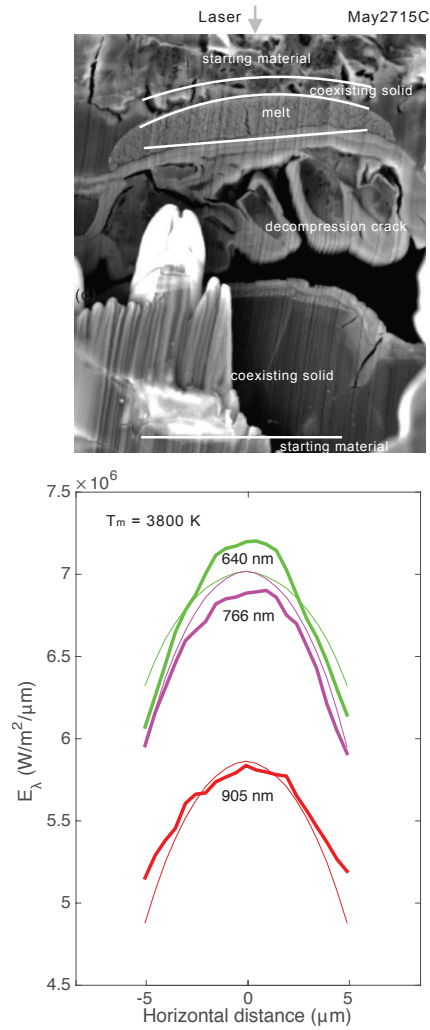


**FIG. S3. (Top panel)** Scanning electron microscopic image of the cross section of sample May2715C with solid lines delineating the boundaries between the five different layers. **(Bottom panel)** The corresponding inverse modeling results. The thick lines are the horizontal intensities of the radiation detected and the thin lines are the fitted results with corresponding wavelength labeled. Note, only three wavelengths are fit (i.e., 640, 766 and 905 nm) to determine  $T_m = 3800 \text{ K}$ .

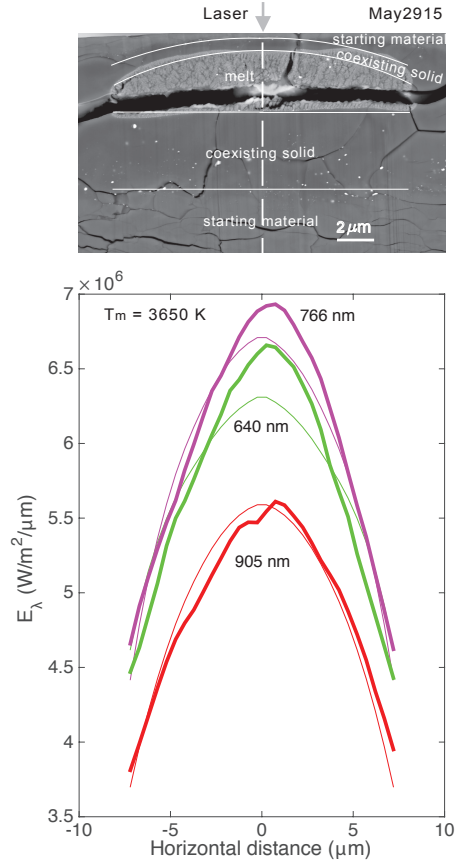


**FIG. S4. (Top panel)** Scanning electron microscopic image of the cross section of sample May2915 with solid lines delineating the boundaries between the five different layers. **(Bottom panel)** The corresponding inverse modeling results. The thick lines are the horizontal intensities of the radiation detected and the thin lines are the fitted results with corresponding wavelength labeled. Note, only three wavelengths are fit (i.e., 640, 766 and 905 nm) to determine  $T_m = 3650$  K.

<sup>1</sup>A. F. Goncharov, V. V. Struzhkin, and S. D. Jacobsen, *Science* **312**, 1205 (2006).

<sup>2</sup>A. F. Goncharov, B. D. Haugen, V. V. Struzhkin, P. Beck, and S. D. Jacobsen, *Nature* **456**, 231 (2008).

<sup>3</sup>A. F. Goncharov, P. Beck, V. V. Struzhkin, B. D. Haugen, and S. D. Jacobsen, *Physics of the Earth and Planetary Interiors* **174**, 24 (2009).

<sup>4</sup>A. F. Goncharov, V. V. Struzhkin, J. A. Montoya, S. Kharlamova, R. Kundargi, J. Siebert, J. Badro, D. Antonangeli, F. J. Ryerson, and W. Mao, *Physics of the Earth and Planetary Interiors* **180**, 148 (2010).